



In situ observation of nanoparticle formation in nickel-based mechanical alloyed powders

Man Wang^{1,2} , Heung Nam Han² , Hee-Suk Chung³ , Young-Bum Chun¹ , and Jinsung Jang^{1,*}

¹Advanced Materials Development Team, Korea Atomic Energy Research Institute, Daejeon 34057, Republic of Korea

²Department of Materials Science and Engineering, Research Institute of Advanced Materials, Seoul National University, Seoul 08826, Republic of Korea

³Jeonju Center, Korea Basic Science Institute, Jeonju 54907, Republic of Korea

Received: 18 April 2018

Accepted: 30 July 2018

Published online:

3 August 2018

© Springer Science+Business Media, LLC, part of Springer Nature 2018

ABSTRACT

Nickel alloy powders with additions of Gd₂O₃ and Ti were mechanically alloyed (MA) using a high-energy ball mill. The formation behaviors of nanoparticles in nickel-based MA powders were investigated using in situ characterization methods, including high-temperature X-ray diffraction and in situ transmission electron microscope (TEM). The added Gd₂O₃ particles were dissolved into the matrix during MA process. Recrystallization of the MA powders occurred between 810 and 880 °C, followed by grain growth. Precipitation of nanoparticles was observed after grain growth using in situ TEM and was attributed to the reduced dislocations and grain boundary area. More importantly, these nanoparticles were dissolved into matrix after the specimen was reheated to a higher temperature of 1014 °C. During subsequent cooling, Gd₂TiO₅ particles were re-precipitated in a more uniform way, including smaller average size of 6.8 nm and reduced interparticle spacing of 26.9 nm.

Introduction

Oxide dispersion strengthened (ODS) alloys are considered promising candidate materials for nuclear applications because of their good high-temperature creep property and excellent irradiation resistance [1–3]. The superior properties of ODS alloys are attributed to the fact that the dispersed nanoparticles can serve as obstacles to dislocation movement [4–6] and also as effective sinks for irradiation-induced defects [7, 8]. Therefore, it is important to understand the formation behaviors of nanoparticles in order to

tailor the microstructure and optimize the properties of ODS alloys.

Regarding the formation behaviors of nanoparticles in ODS alloys, the dissolution of added oxide particles during mechanical alloying (MA) process and the re-precipitation of nanoparticles during subsequent consolidation are widely accepted [1]. Okuda et al. [9] confirmed this mechanism firstly by studying the behavior of Fe–13Cr–3Ti–3Y₂O₃ (wt%, unless noted otherwise) using X-ray diffraction (XRD). They reported that the MA powders displayed no Y₂O₃ peaks, whereas Y₂TiO₅ and Y₂Ti₂O₇

Address correspondence to E-mail: jjang@kaeri.re.kr

peaks were identified after annealing at 1000 °C for 1 h. Alinger et al. [10, 11] reported that Y_2O_3 dissolved in Fe–14Cr-based MA powders, and that nanoparticles precipitated after hot isostatic pressing (HIP) at 850 °C using small-angle neutron scattering (SANS). By using neutron diffraction, Zhang et al. [12] found that 10% of Y_2O_3 was dissolved into ferrite matrix following MA process, and that Y_2O_3 precipitated after annealing at 900 °C. Similar results are also reported using atom probe tomography (APT) and transmission electron microscope (TEM) [13–16]. However, other researchers did not observe any change in the lattice parameters of the matrix and hence concluded that the added oxides did not dissolve into the matrix during MA process [17, 18]. This is also supported by the existence of a Y–O bond in MA powders composed of Fe–9Cr–15 Y_2O_3 [19], as well as the identification of amorphous Y_2O_3 in milled Fe–25 Y_2O_3 powders [20]. Based on these results, an alternative theory is proposed, involving fragmentation of the initial oxide particles into amorphous or nanocrystalline.

Although much progress has been achieved in understanding the formation behaviors of nanoparticles in ODS alloys using various techniques, some uncertainties and limitations still remain. Firstly, previous studies mostly employed ex situ characterization, and therefore information on the early stage and the sequential events that lead to formation of nanoparticles were not covered. Furthermore, very high fractions of oxides (10–25%) were used, especially in studies that claimed formation of amorphous phase. This may lead to some misunderstanding, since the solubility of oxide-forming elements in ferrite is very low.

In this study, the formation behaviors of nanoparticles in nickel-based MA powders were investigated using high-temperature XRD and in situ TEM. As lanthanide oxides are suggested as an effective dispersion source for nickel alloys based on density functional calculation [21], Gd_2O_3 was added to nickel alloy powders in this study. The high-temperature XRD analysis gave statistical data on the bulky powder sample, and in situ TEM observation revealed the sequential events that led to the formation of nanoparticles.

Materials and methods

Pre-alloyed Ni–Cr–Fe powders with average size of 45 μm were used as the base material. Gd_2O_3 powders with sizes of 15–30 nm and Ti powders with average size of 45 μm were blended with the pre-alloyed powders. The nominal composition was Ni–30Cr–11Fe–0.50Ti–1.36 Gd_2O_3 (wt%). MA was carried out using a horizontal ball mill (Zoz Simoloyer CM08TM) under argon atmosphere. The capacity of the processing chamber was 8 L, and the total load of raw powders was 1000 g. 100Cr6 steel balls with diameter of 5 mm were used as grinding media, and the ball-to-powder weight ratio was 10:1. In order to avoid overheating, the MA process was performed in a cyclic mode, comprising 5 min at 50 rpm, 40 min at 200 rpm, 10 min at 20 rpm and 5 min pause. Sixty cycles were carried out in this study, giving a total milling time of 40 h at 200 rpm.

High-temperature XRD was performed using a PANalytical Empyrean diffractometer (Cu $K\alpha$ radiation, $\lambda = 1.54056 \text{ \AA}$) at 45 kV and 40 mA with a step size of 0.0131° . XRD measurements were taken at room temperature (RT), and then at high temperatures between 600 and 1000 °C in vacuum (10^{-4} to 10^{-3} Pa). Rietveld analysis was carried out on the whole XRD patterns using FullProf program. The broadening of peaks for matrix was estimated using a

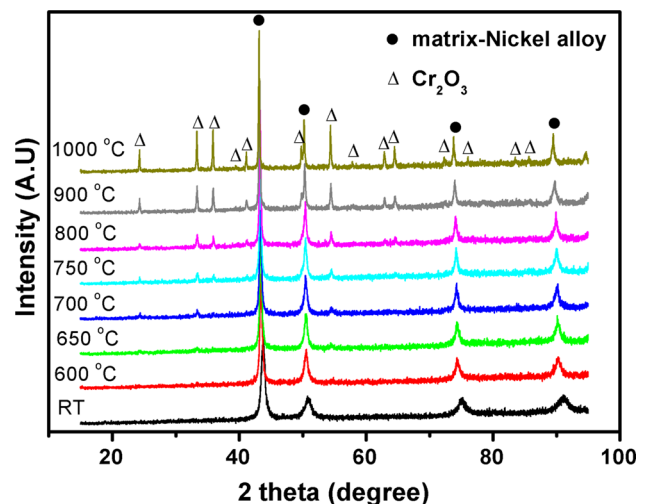


Figure 1 XRD patterns of nickel-based MA powders at different temperatures.

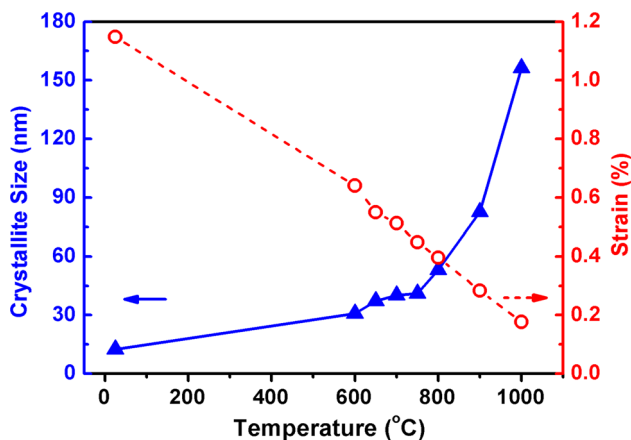
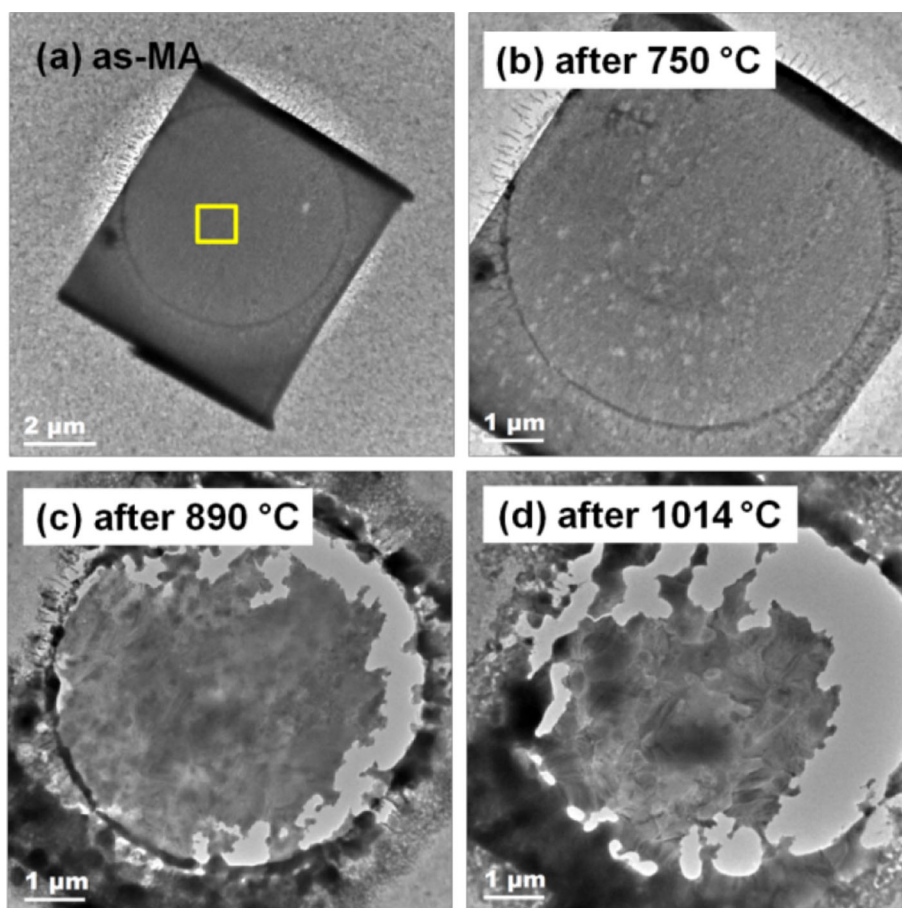


Figure 2 Evolution of crystallite size and strain of nickel alloy phase with temperature.

pseudo-Voigt function, and then the crystallite size and strain were obtained [22, 23].

Microstructure evolution was investigated using in situ TEM (JEOL-ARM 200F) with an in situ sample holder (Aduro 500). The TEM specimen was prepared from the MA powders using a dual focused ion beam

Figure 3 BF-TEM images of MA powders after heating to different temperatures. **a** As-MA powder, **b** after 750 °C, **c** after 890 °C, **d** after 1014 °C.



(FIB, Nova 200). The evolution of the microstructure was recorded in real time during the heating and cooling processes. When a significant change in microstructure was observed, the heating process was stopped and the specimen was cooled to RT to allow detailed examination. Afterward, the specimen was heated again to a higher temperature, and the microstructure evolution of the same area was recorded. The real-time temperature of the specimen was measured across the viewing area by Protochips' Clarity™ software with a tolerance of 1.3%. The heating and cooling rate was both 1 °C s⁻¹.

Results

High-temperature X-ray diffraction

Figure 1 shows XRD patterns of the nickel-based MA powders at different temperatures. The as-MA powders only exhibited diffraction peaks of nickel alloy, which were somewhat broad due to the fine crystallite size and strain introduced during the MA process. With

increasing temperature, the matrix peaks increased in height and turned to be sharper. Also, faint Cr_2O_3 peaks began to appear at 650 °C, and they became more obvious with increasing temperature. Rietveld refinement was performed on the whole XRD patterns, and Fig. 2 shows the evolution of crystallite size and strain of the matrix phase with temperature. The as-MA powders exhibited a fine crystallite size of approximately 12.5 nm and a large strain of 1.1%. The strain was gradually relieved with increasing temperature. The crystallite size remained around 50 nm up to 800 °C and then started to increase significantly above 800 °C.

In situ microstructure observation

Figure 3 presents bright-field (BF) TEM images showing the overall microstructure evolution of MA powders after heating to different temperatures, such

as 750 °C, 890 °C and 1014 °C (Fig. 3b–d). The area marked by a square in Fig. 3a was chosen for in situ observation, and the microstructure characterization was focused on this area.

Characterization of as-MA powders

Figure 4 shows TEM micrographs of the as-MA powders. The different contrasts shown in the BF-TEM image (Fig. 4a) were due to strain accumulation during the MA process. The EDS mapping results show that all the alloying elements were uniformly distributed, except for several Ti-rich regions (~ 20 nm) as indicated by the arrows in Fig. 4b. The size of Ti-rich regions was much smaller than that of the originally added Ti powders ($\sim 45 \mu\text{m}$); therefore, these Ti-rich regions may be remnants of Ti powders during the MA process. Figure 4c shows a

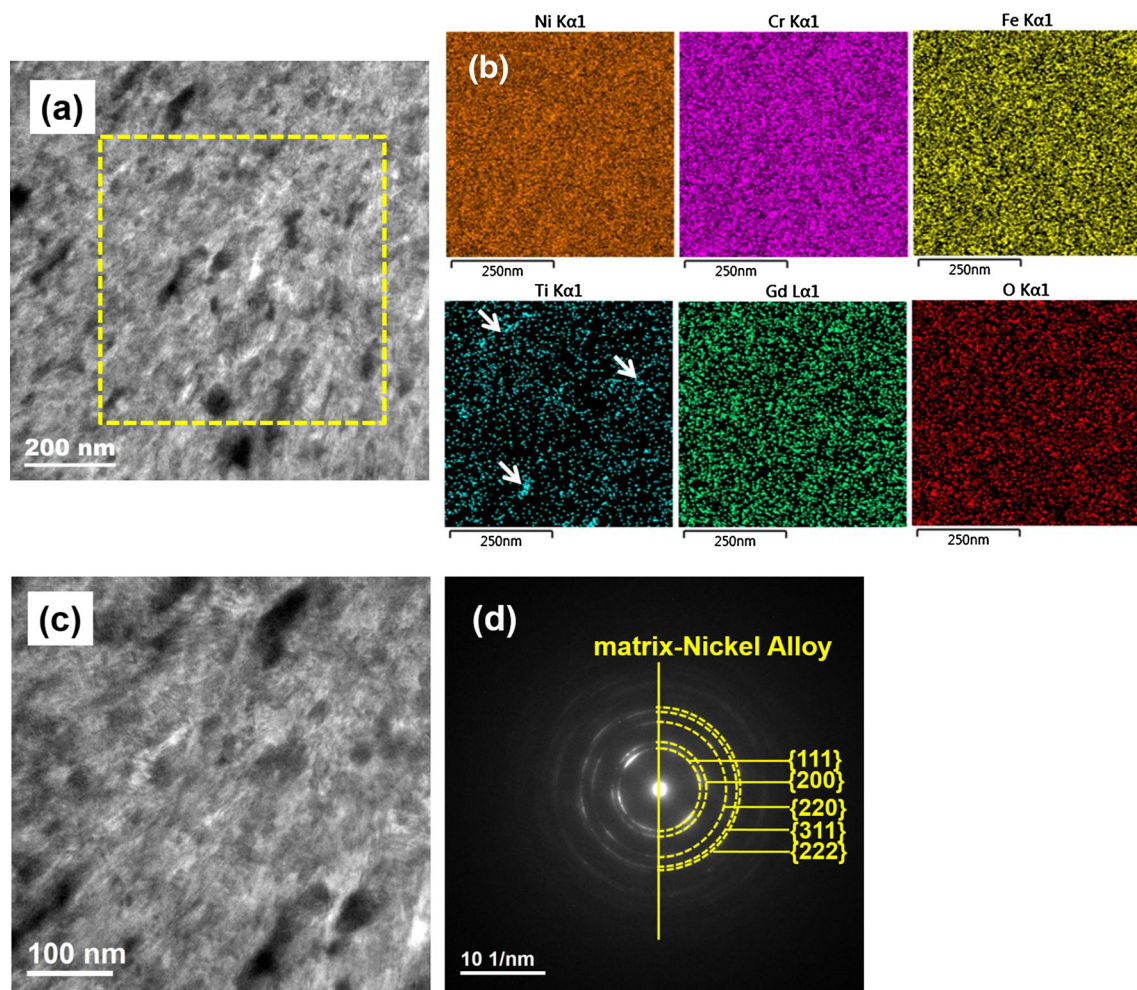
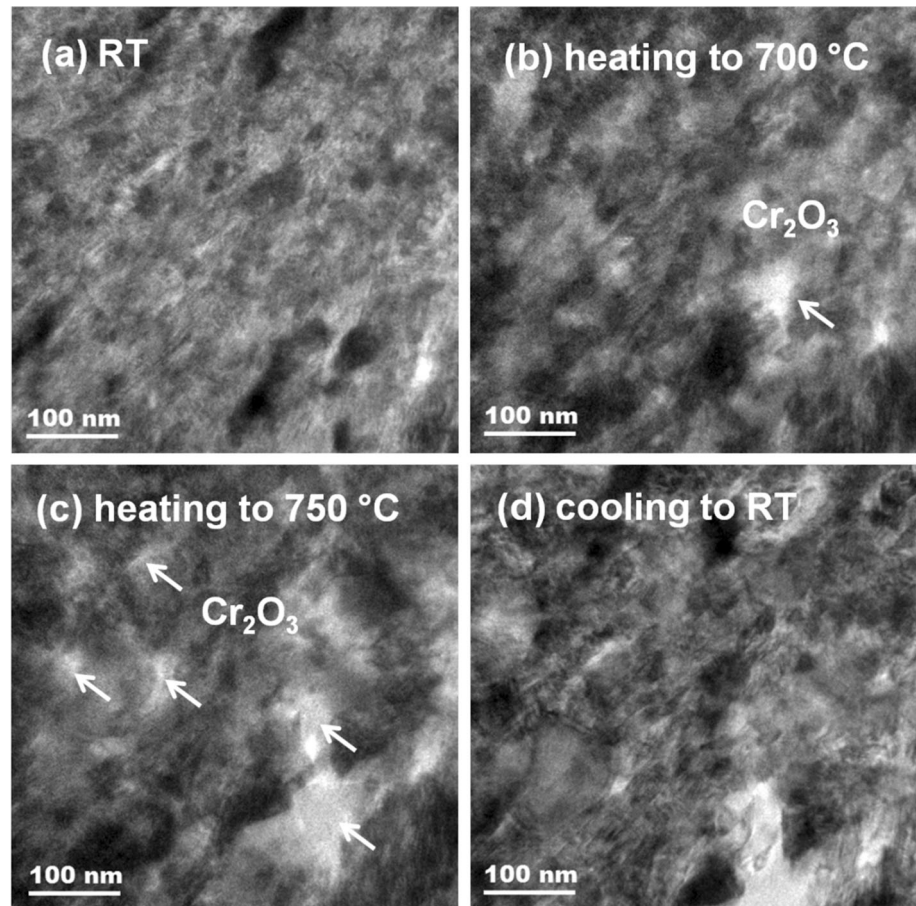


Figure 4 TEM results of as-MA powders. **a** BF-TEM image, **b** EDS mapping results of the region within the rectangle in (a), **c** BF-TEM image of in situ observing area, **d** SADP corresponding to (c).

Figure 5 Snapshots of MA powders during heating to 750 °C. **a** RT, **b** heating to 700 °C, **c** heating to 750 °C, **d** cooling down to RT.



larger amplification of Fig. 4a and was selected for in situ observation. Its selected area electron diffraction pattern (SADP) corresponded to nickel alloy phase, as shown in Fig. 4d. Based on the EDS mapping and SADP results, it is concluded that the added Gd_2O_3 was dissolved into matrix during the MA process.

Microstructure evolution of MA powders during heating and cooling

Figure 5 shows snapshots of the MA powders during heating to 750 °C, and after cooling to RT. Cr_2O_3 phase appeared to form when the specimen was heated to around 700 °C (indicated by the arrows in Fig. 5b), and its content increased with increasing temperature (Fig. 5c). The TEM results of Cr_2O_3 phase were consistent with the XRD results shown in Fig. 1. The Cr_2O_3 phase was between 50 and 150 nm in size. The formation of Cr_2O_3 was due to the high content of Cr (~ 30 wt%) in the matrix and its great affinity for oxygen. Williams et al. [24] also reported

the formation of Cr_2O_3 in Fe–14Cr–2 W-based ODS alloy after annealing at 800 °C.

Figure 6 shows snapshots of the MA powders during reheating from RT to 890 °C. Recrystallization appeared to start at around 810 °C (Fig. 6b). The contrast became clearer as the strain was relieved. Recrystallization seemed to finish at around 880 °C, and the grain size was between 60 and 100 nm, as shown in Fig. 6c. The XRD results (Fig. 2) show that the crystallite sizes at 800 °C and 900 °C were 53 and 83 nm, respectively, which matched well with the TEM results. The grains then coarsened through grain boundary migration, and the open arrow in Fig. 6e indicates the migration direction of a grain boundary. Precipitates appeared after grain coarsening (Fig. 6f). The heating process was stopped after reaching 890 °C, and the specimen was cooled to RT in order to examine the precipitates.

Figure 7a is a BF-TEM image showing many particles distributed in the grain interior. Figure 7b is a high-angle annular dark field (HAADF) STEM image showing a clear Z-contrast. According to the EDS

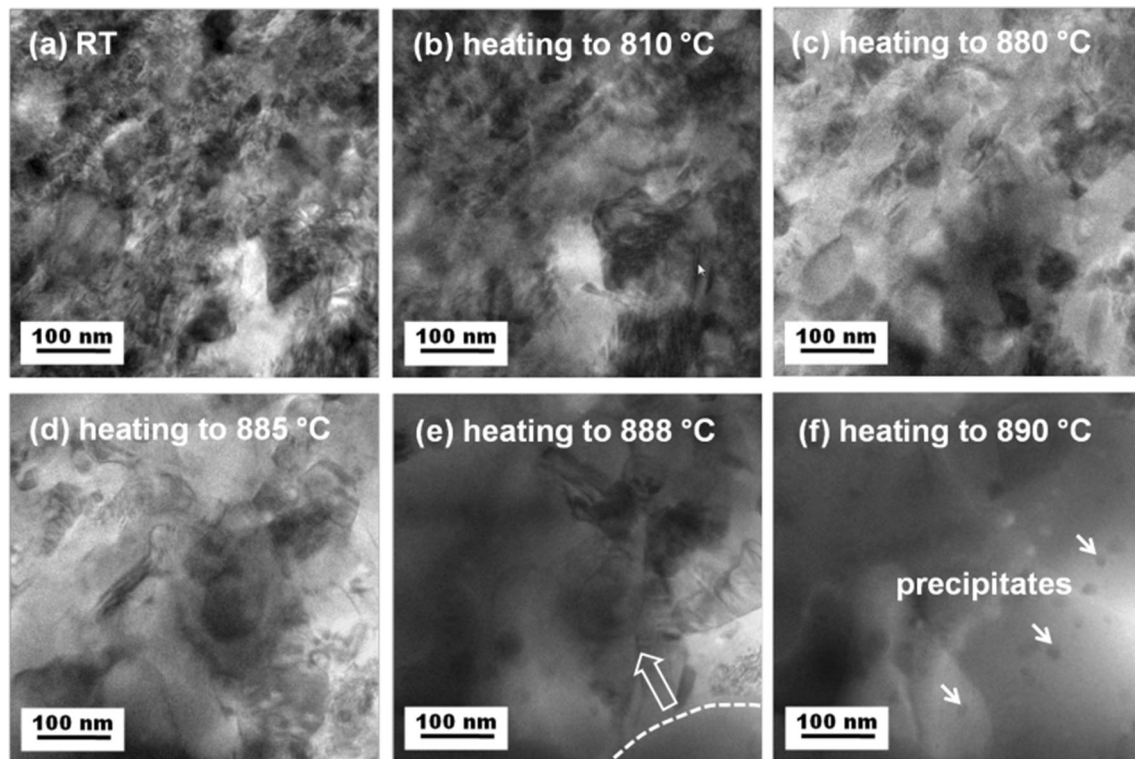


Figure 6 Snapshots of MA powders during reheating to 890 °C. **a** RT, **b** heating to 810 °C, **c** heating to 880 °C, **d** heating to 885 °C, **e** heating to 888 °C, **f** heating to 890 °C.

mapping results (Fig. 7c), the gray particles were rich in Ti (indicated by the arrows in Fig. 7c), while the bright particles were rich in Gd (indicated by the circles in Fig. 7c). The Ti-rich particles were approximately 20 nm in size, which was similar to that of the Ti-rich regions in as-MA powders (Fig. 4b). It seems that the Ti-rich regions did not change during reheating to 890 °C. As shown in Fig. 8, particles of Gd_2O_3 (cubic, #98-002-7996) and Gd_2TiO_5 (orthorhombic, 98-016-2128) were identified, respectively, based on the HR-TEM analysis. Figure 7d shows that these particles had a relatively broad size distribution. The average particle size and interparticle spacing were 13.5 and 71.9 nm, respectively.

The MA powders were then reheated to 1014 °C and the resulting microstructure evolution is shown in Fig. 9. Small particles were dissolved first when reaching 920 °C (Fig. 9b), and most particles were dissolved after annealing at 920 °C for 70 s (Fig. 9c). The white-contrast features, indicated by the arrows in Fig. 9c, were voids, which will be analyzed later. The circle in Fig. 9c indicates a large Cr_2O_3 particle, which was dissolved at around 1000 °C. The matrix

was kind of defect-free after the specimen was reheated to 1014 °C, and then the specimen was cooled to RT. Particles were re-precipitated during subsequent cooling, mainly between 900 and 800 °C (Fig. 9e, f).

Figure 10a is an underfocus BF-TEM image. Voids exhibit dark Fresnel fringe at underfocused condition [25]; therefore, the features indicated by the arrows in Fig. 10a were identified as voids. These voids showed black contrast in the HAADF-STEM image, with average size of 13.2 ± 3.8 nm. It should be noted that the majority of the particles in Fig. 10b exhibited bright contrast and were identified as Gd_2TiO_5 based on HR-TEM analysis (Fig. 10c, d). These particles exhibited a much narrower size distribution, with smaller average size of 6.8 nm and reduced interparticle spacing of 26.9 nm (Fig. 10f).

Discussion

Analysis of as-MA powders

The crystallite size and strain of as-MA powders were 12.5 nm and 1.1%, respectively. Nanostructure and large strain are typical features of MA powders,

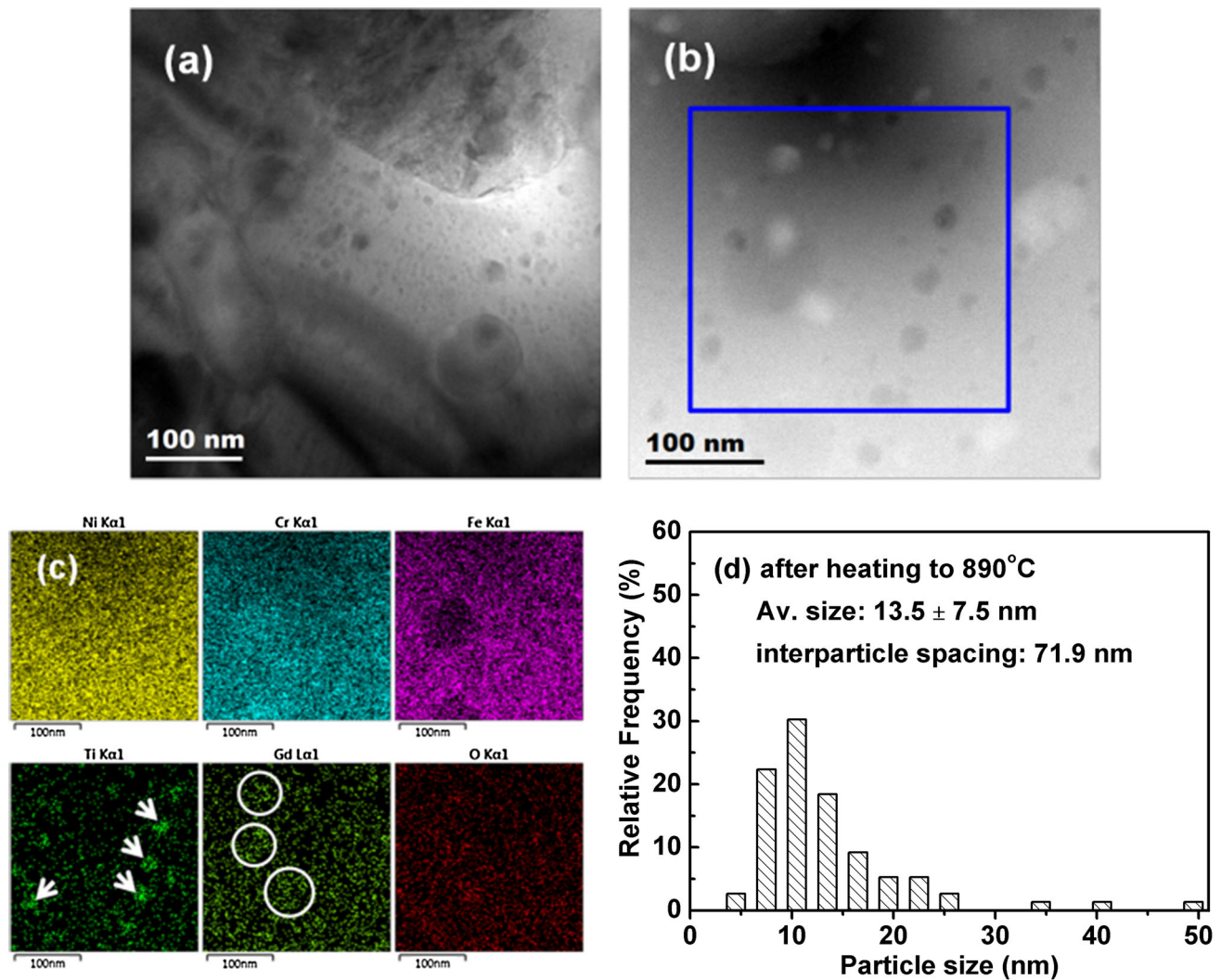


Figure 7 TEM results of MA powders after reheating to 890 °C. **a** BF-TEM image, **b** HAADF-STEM image, **c** EDS mapping results corresponding to the rectangular region in **(b)**, **d** particle size distribution.

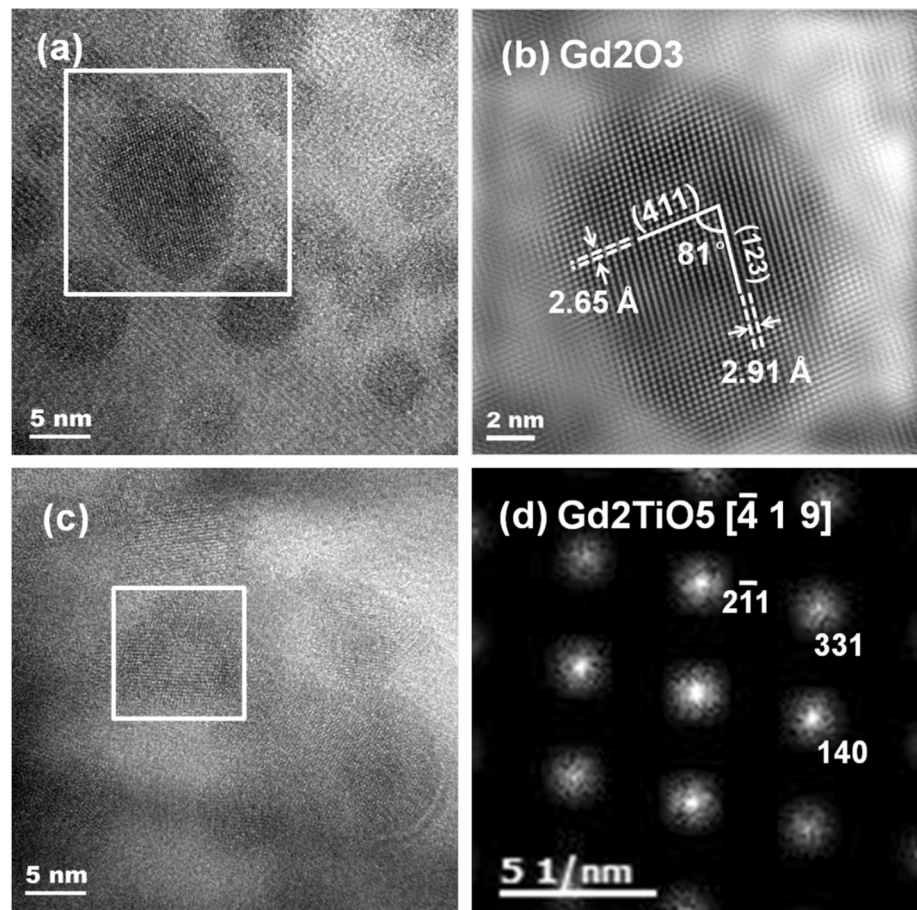
since the blended powders are repeatedly flattened, cold welded, fractured, and rewelded during MA process [26–29]. Shear bands containing high density of dislocations are introduced by the heavy deformation and develop into subgrains that are separated by low-angle grain boundaries. On further milling, these low-angle grain boundaries will be replaced by high-angle grain boundaries to reduce the lattice strain, resulting in refinement of grain size. At the same time, other crystal defects such as vacancies and dislocations are introduced, which can be explained by the large strain within as-MA powders. The increased grain boundaries and dislocations contribute to extend the solubility of oxide-forming elements in the matrix. In this study, the TEM results indicated that the added Gd_2O_3 particles were

dissolved into matrix during MA process. Then, the as-MA powders became supersaturated solid solution with oxide-forming elements and oxygen atoms.

Precipitation behaviors of nanoparticles in MA powders

Different particles were observed and identified after reheating to 890 °C, comprising Ti (~ 20 nm), Gd_2O_3 (~ 15 nm) and Gd_2TiO_5 (~ 8 nm). The Ti particles may be the Ti-rich regions in the as-MA powders considering their similar size, while the particles of Gd_2O_3 and Gd_2TiO_5 were precipitated from the matrix. The precipitation of nanoparticles was related to strain recovery and grain coarsening. As shown in Fig. 2, the strain recovered gradually with increasing

Figure 8 TEM characterization of particles in MA powders after reheating to 890 °C. **a** HR image of particles, **b** inverse FFT image of rectangle area in (a), **c** HR image of particles, **d** FFT image of rectangle area in (c).



temperature, indicating that the crystal defects were annealed and annihilated. Moreover, grains coarsened after recrystallization at around 880 °C (Fig. 6c–f), thereby decreasing the grain boundary area. As a result, the solubility of decomposed atoms in matrix would be reduced due to the decrease in crystal defects, resulting in precipitation of nanoparticles. In the present study, in situ TEM observations provide direct experimental evidence for nanoparticle precipitation.

The precipitated particles were successively dissolved into matrix during reheating from 920 to 1014 °C (Fig. 9b–d), and then finer particles were reprecipitated from the supersaturated matrix during subsequent cooling, mainly between 900 and 800 °C (Fig. 9e, f). These particles were identified as Gd_2TiO_5 (Fig. 10). Voids were observed during reheating to 1014 °C, with average size of about 13.2 nm. Void formation has been widely reported in other ODS materials and is usually attributed to the absorbed gas from milling atmosphere during MA process [30–32]. Voids were also found in the Al–Al₂O₃

nanocomposites and were ascribed to the compressibility behavior of the materials during MA process [33, 34].

Only Gd_2TiO_5 particles were observed after reheating to 1014 °C, whereas three kinds of particles (Ti, Gd_2O_3 and Gd_2TiO_5) were observed after reheating to 890 °C. The designed atomic ratio of Gd:Ti was 2:3. However, some Ti-rich regions were present in the as-MA powders, indicating that some of the Ti powders were not fully dissolved into the matrix during MA process. Although quantitative analysis is not simple for this case, it could be assumed that the dissolved Ti atoms were relatively deficient and consequently resulted in the formation of Gd_2O_3 and Gd_2TiO_5 . Nevertheless, all the pre-existing and precipitated particles were dissolved into matrix during reheating to 1014 °C and were then reprecipitated in the form of Gd_2TiO_5 during subsequent cooling.

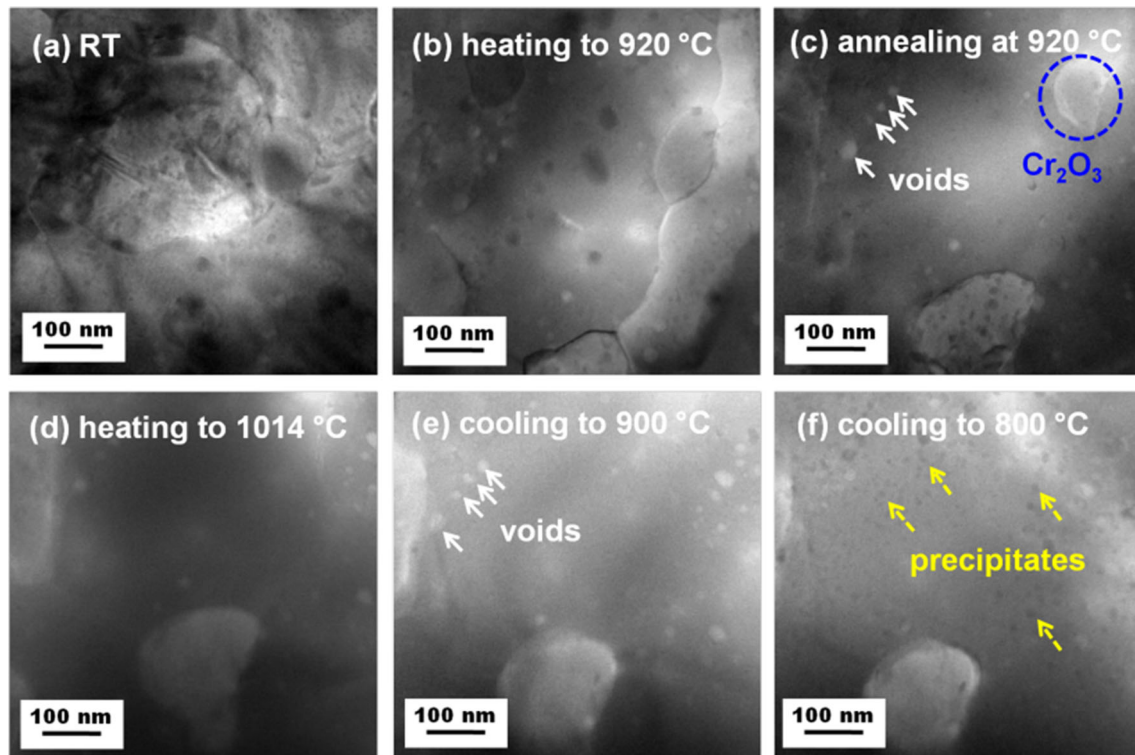


Figure 9 Snapshots of MA powders during reheating to 1014 °C. **a** RT, **b** heating to 920 °C, **c** annealing at 920 °C for 70 s, **d** heating to 1014 °C, **e** cooling to 900 °C, **f** cooling to 800 °C.

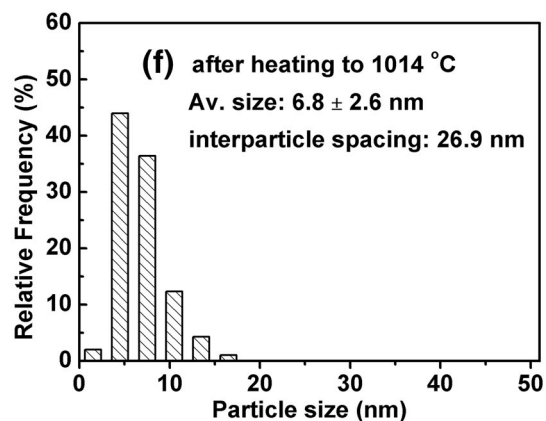
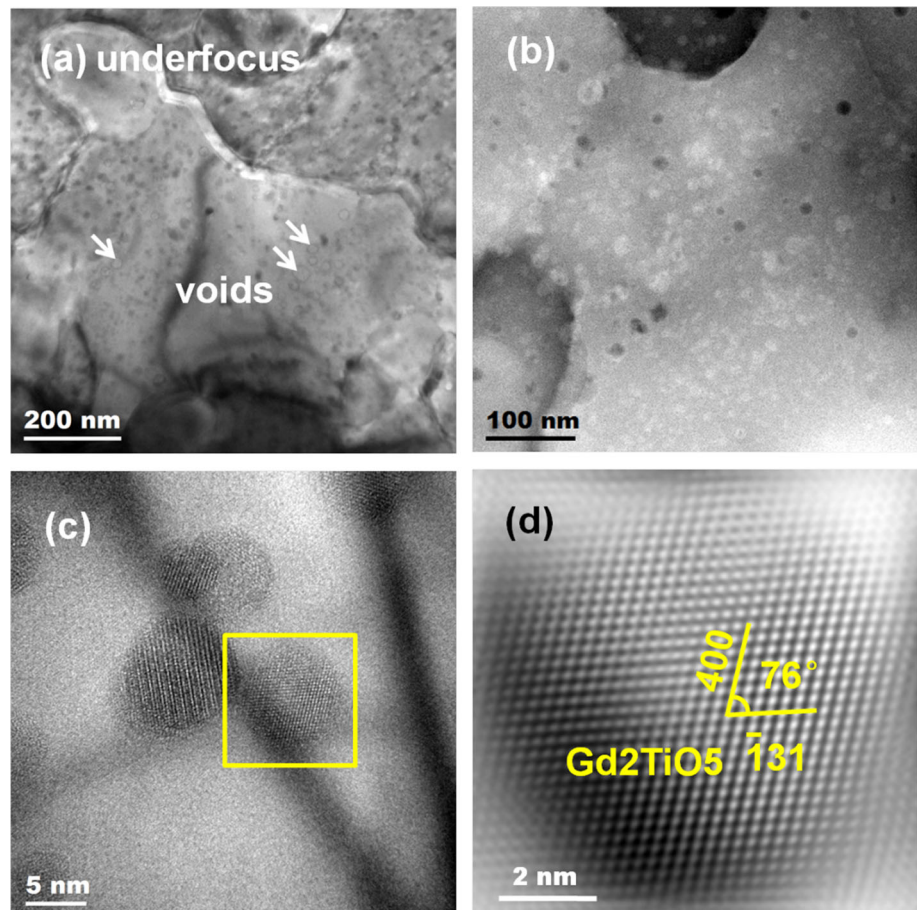
Improved uniformity of nanoparticle distribution

Compared with reheating to 890 °C (Fig. 7d), the nanoparticles were distributed more uniformly after reheating to 1014 °C (Fig. 10f). The average particle size and interparticle spacing after reheating to 1014 °C were 6.8 and 26.9 nm, respectively, compared with 13.5 and 71.9 nm after reheating to 890 °C. The more uniform distribution of finer precipitates may be associated with the microstructure change of supersaturated matrix. As discussed in “Precipitation behaviors of nanoparticles in MA powders” section, the precipitation of particles during reheating to 890 °C was related to strain recovery and grain coarsening. The high-temperature XRD results (Fig. 2) show that approximately 66% of the strain was relieved at 800 °C, indicating that a great number of crystal defects were annealed and annihilated. Some precipitates would be developed first, as the solubility of decomposed atoms in matrix was reduced due to the decreased defects. On further heating, the grain boundary area was decreased due to grain coarsening after recrystallization at 880 °C

(Fig. 6d–f), and the solubility of decomposed atoms was reduced further, resulting in more precipitates. The particles that precipitated first, as a result of strain recovery at relatively low temperature, would experience growth during the continuous heating process. Therefore, particles were precipitated at different stages during heating to 890 °C, resulting in a broad size distribution of particles with larger average size of 13.5 nm (Fig. 7d).

After reaching 1014 °C, all the precipitates were successively dissolved into matrix, and the matrix became supersaturated again. The high-temperature XRD results indicate that strain was relieved to a very low level at 1000 °C (Fig. 2). That is to say, the dissolution of oxide particles is not due to dislocations or grain boundaries, which can extend the solubility of oxide-forming elements in matrix. The dissolution of precipitates between 920 and 1014 °C may be related to the extended solubility arising from higher temperature. As the solubility declined during subsequent cooling, nanoparticles were re-precipitated from the supersaturated matrix, mainly between 900 and 800 °C, resulting in more uniformly distributed precipitates.

Figure 10 TEM characterization of particles in MA powders after reheating to 1014 °C. **a** Underfocused BF-STEM image, **b** HAADF-TEM image showing distribution of particles, **c** HR image of particles, **d** inverse FFT image of the rectangle area in (c), **f** particle size distribution.



Conclusions

Nickel alloy powders with practical additions of Gd_2O_3 and Ti were mechanically alloyed using a high-energy ball mill. The formation behaviors of nanoparticles were investigated using high-temperature XRD and in situ TEM. The following conclusions can be drawn:

- (1) The as-MA powders exhibited fine grain structure (12.5 nm) and large strain of 1.1% associated with crystal defects, both of which attributed to extend the solubility of oxide-forming elements in matrix.
- (2) Two kinds of nanoparticle precipitation processes were observed directly by in situ TEM. Precipitation during reheating to 890 °C was closely related to strain recovery and grain

growth, which reduced the solubility of decomposed atoms in matrix. Precipitation of nanoparticles was also observed during cooling from 1014 °C to RT, mainly between 900 and 800 °C. This was because the solubility of decomposed atoms in the matrix declined with decreasing temperature.

- (3) More uniform distribution of Gd₂TiO₅ particles, with smaller size of 6.8 nm and reduced inter-particle spacing of 26.9 nm, was achieved after the specimen was reheated to 1014 °C. The more uniform distribution of precipitates may be associated with the different microstructures of the supersaturated matrix. This suggests that appropriate heat treatment of MA powders could produce ODS alloys with more uniform distribution of finer particles.

Acknowledgements

This study was supported by the Institute's R&D Program of Korea Atomic Energy Research Institute (KAERI). H.N. Han was supported by the National Research Foundation of Korea (NRF) granted by the Korea government (MSIT) (No. NRF-2015R1A5A1037627). The authors would like to thank Dr. Ki-Myung Song and Dr. Seongsu Lee of Neutron Science Center of KAERI for carrying out the high-temperature XRD experiment and valuable discussion on the results.

Compliance with ethical standards

Conflict of interest The authors certify that we have no affiliations with or involvement in any organization or entity with any financial interest or non-financial interest in the subject matter or materials discussed in this manuscript.

References

- [1] Ukai S, Fujiwara M (2002) Perspective of ODS alloys application in nuclear environments. *J Nucl Mater* 307:749–757
- [2] Murty K, Charit I (2008) Structural materials for Gen-IV nuclear reactors: challenges and opportunities. *J Nucl Mater* 383(1–2):189–195
- [3] Zinkle SJ, Was G (2013) Materials challenges in nuclear energy. *Acta Mater* 61(3):735–758
- [4] Herrick R, Weertman J, Petkovic-Luton R, Luton M (1988) Dislocation/particle interactions in an oxide dispersion strengthened alloy. *Scr Metall* 22(12):1879–1884
- [5] Zakine C, Prioul C, Francois D (1996) Creep behaviour of ODS steels. *Mater Sci Eng, A* 219(1–2):102–108
- [6] Nganbe M, Heilmaier M (2004) Modelling of particle strengthening in the γ' and oxide dispersion strengthened nickel-base superalloy PM3030. *Mater Sci Eng A* 387:609–612
- [7] Oono N, Ukai S, Kondo S, Hashitomi O, Kimura A (2015) Irradiation effects in oxide dispersion strengthened (ODS) Ni-base alloys for Gen. IV nuclear reactors. *J Nucl Mater* 465:835–839
- [8] Zinkle S, Boutard J, Hoelzer D, Kimura A, Lindau R, Odette G, Rieth M, Tan L, Tanigawa H (2017) Development of next generation tempered and ODS reduced activation ferritic/martensitic steels for fusion energy applications. *Nucl Fusion* 57(9):092005
- [9] Okuda T, Fujiwara M (1995) Dispersion behaviour of oxide particles in mechanically alloyed ODS steel. *J Mater Sci Lett* 14(22):1600–1603
- [10] Alinger M, Odette G, Hoelzer D (2004) The development and stability of Y–Ti–O nanoclusters in mechanically alloyed Fe–Cr based ferritic alloys. *J Nucl Mater* 329:382–386
- [11] Alinger M, Odette G, Hoelzer D (2009) On the role of alloy composition and processing parameters in nanocluster formation and dispersion strengthening in nanostructured ferritic alloys. *Acta Mater* 57(2):392–406
- [12] Zhang H, Gorley MJ, Chong KB, Fitzpatrick ME, Roberts SG, Grant PS (2014) An in situ powder neutron diffraction study of nano-precipitate formation during processing of oxide-dispersion-strengthened ferritic steels. *J Alloys Compd* 582:769–773
- [13] Zhang L, Ukai S, Hoshino T, Hayashi S, Qu X (2009) Y₂O₃ evolution and dispersion refinement in Co-base ODS alloys. *Acta Mater* 57(12):3671–3682
- [14] Laurent-Brocq M, Legendre F, Mathon M-H, Mascaro A, Poissonnet S, Radiguet B, Pareige P, Loyer M, Leseigneur O (2012) Influence of ball-milling and annealing conditions on nanocluster characteristics in oxide dispersion strengthened steels. *Acta Mater* 60(20):7150–7159
- [15] Saber M, Xu W, Li L, Zhu Y, Koch CC, Scattergood RO (2014) Size effect of primary Y₂O₃ additions on the characteristics of the nanostructured ferritic ODS alloys: comparing as-milled and as-milled/annealed alloys using S/TEM. *J Nucl Mater* 452(1):223–229

- [16] He P, Gao P, Tian Q, Lv J, Yao W (2017) An in situ SANS study of nanoparticles formation in 9Cr ODS steel powders. *Mater Lett* 209:535–538
- [17] Toulbi L, Ratti M, André G, Onimus F, De Carlan Y (2011) Use of neutron and X-ray diffraction to study the precipitation mechanisms of oxides in ODS materials. *J Nucl Mater* 417(1):225–228
- [18] Hilger I, Tegel M, Gorley M, Grant P, Weißgärber T, Kieback B (2014) The structural changes of Y_2O_3 in ferritic ODS alloys during milling. *J Nucl Mater* 447(1):242–247
- [19] Dai L, Liu Y, Dong Z (2012) Size and structure evolution of yttria in ODS ferritic alloy powder during mechanical milling and subsequent annealing. *Powder Technol* 217:281–287
- [20] Liu T, Shen H, Wang C, Chou W (2013) Structure evolution of Y_2O_3 nanoparticle/Fe composite during mechanical milling and annealing. *Prog Nat Sci Mater Int* 23(4):434–439
- [21] Hong K-H, Kim JH, Chang K, Kwon J (2016) Prediction of potential candidates for dispersion strengthening materials in Ni based alloys. *Comput Mater Sci* 117:215–220
- [22] Rodríguez-Carvajal J (2003) Study of micro-structural effects by powder diffraction using the program FULLPROF. Laboratoire Léon Brillouin (CEA-CNRS), CEA/Saclay 91191
- [23] Rietveld H (1969) A profile refinement method for nuclear and magnetic structures. *J Appl Crystallogr* 2(2):65–71
- [24] Williams CA, Unifantowicz P, Baluc N, Smith GD, Marquis EA (2013) The formation and evolution of oxide particles in oxide-dispersion-strengthened ferritic steels during processing. *Acta Mater* 61(6):2219–2235
- [25] Williams DB, Carter CB (1996) The transmission electron microscope. In: *Transmission electron microscopy*. Springer, Boston, pp 3–17
- [26] Suryanarayana C (2001) Mechanical alloying and milling. *Prog Mater Sci* 46(1):1–184
- [27] Fathy A, Wagih A, El-Hamid MA, Hassan A (2013) Effect of mechanical milling on the morphology and structural evaluation of Al– Al_2O_3 nanocomposite powders. *Int J Eng Trans A Basics* 27(4):625
- [28] Wagih A (2015) Mechanical properties of Al–Mg/ Al_2O_3 nanocomposite powder produced by mechanical alloying. *Adv Powder Technol* 26(1):253–258
- [29] Wagih A (2016) Synthesis of nanocrystalline Al_2O_3 reinforced Al nanocomposites by high-energy mechanical alloying: microstructural evolution and mechanical properties. *Trans Indian Inst Met* 69(4):851–857
- [30] Chen Y, Jones A, Miller U (2002) Origin of porosity in oxide-dispersion-strengthened alloys produced by mechanical alloying. *Metall Mater Trans A* 33(8):2713–2718
- [31] Ortega Y, Monge M, De Castro V, Muñoz A, Leguey T, Pareja R (2009) Void formation in ODS EUROFER produced by hot isostatic pressing. *J Nucl Mater* 386:462–465
- [32] Capdevila C, Miller MK, Toda I, Chao J (2010) Influence of the α – α' phase separation on the tensile properties of Fe-base ODS PM 2000 alloy. *Mater Sci Eng A* 527(29):7931–7938
- [33] Wagih A, Fathy A (2018) Improving compressibility and thermal properties of Al– Al_2O_3 nanocomposites using Mg particles. *J Mater Sci*. <https://doi.org/10.1007/s10853-018-2422-1>
- [34] Wagih A, Fathy A, Sebaey TA (2016) Experimental investigation on the compressibility of Al/ Al_2O_3 nanocomposites. *Int J Mater Prod Technol* 52(3–4):312–332